Supporting Information

{Ru(CO)$_x$}-core Complexes with Benzimidazole Ligands: Synthesis, X-ray Structure and Evaluation of Anticancer Activity *in Vivo*

Gabriella Tamasi[a]*, Antonello Merlino[b,c], Federica Scaletti[d,e], Petra Heffeter[f,g], Anton A. Legin[h], Michael A. Jakupec[g,h], Walter Berger[f,g], Luigi Messori[d], Bernhard K. Keppler[g,h]*, Renzo Cini[a]

[a] *Department of Biotechnology, Chemistry and Pharmacy, University of Siena, Via Aldo Moro 2, 53100 Siena, Italy. Email: tamasi@unisi.it*

[b] *Department of Chemical Sciences, University of Naples Federico II, Via Cintia, 80126, Napoli, Italy*

[c] *Institute of Biostructure and Bioimaging, CNR, Via Mezzocannone 16, 80120, Napoli, Italy*

[d] *Department of Chemistry, University of Florence, Via della Lastruccia 3-13, 50019 Sesto Fiorentino, Florence, Italy.*

[e] *Department of Chemistry, University of Massachusetts Amherst, 710 Nt. Pleasant Street, Amherst, MA 01003, United States.*

[f] *Institute of Cancer Research, Department of Medicine I, Medical University of Vienna, Borschkegasse 8a, 1090 Vienna, Austria.*

[g] *Research Platform "Translational Cancer Therapy Research", University of Vienna, Währinger Straße 42, 1090 Vienna, Austria.*

[h] *Institute of Inorganic Chemistry, University of Vienna, Währinger Straße 42, 1090 Vienna, Austria. Email: bernhard.keppler@univie.ac.at*

Table S1. Data collection and refinement statistics for the adduct for HEWL-*fac*-[Ru(CO)$_3$Cl$_2$($\underline{N}^3$-MBI)] system (abbreviated, HEWL-RuMBI).

Parameter	HEWL-RuMBI
Crystal System	Tetragonal
Space group	P4(3)2(1)2, no 96
Unit cell parameters	
a,b,c (Å)	78.50, 78.50, 36.31
Molecules per asymmetric unit	1
Observed reflections	35577
Unique reflections	5740
Resolution (Å)	55.51-2.25 (2.29-2.25)
Completeness (%)	99.4 (100)
Rmerge†	0.085 (0.436)
I/σ(I)	12.9 (5.0)
Multiplicity	6.2 (6.3)
Refinement	
Resolution (Å)	55.51-2.25
Number of reflections in working set	5452
Number of reflections in test set	261
R factor/R free (%)	0.152/0.237
Number of non-H atoms	1189
Number of Ru containing fragments	1
Occupancy of Ru atoms	0.8
B-factor of Ru atoms	46.2
Overall B-factor	34.9
Ramachandran values (%)	
Most favored/ Allowed	89.4/9.7
Generously allowed/ Disallowed	0.9/0
R.m.s.d. bonds(Å)	0.020
R.m.s.d. angles(°)	1.93

Table S2. Selected bond distances (Å) and angles (°) for *fac*-[Ru^{II}(CO)$_3$Cl$_2$($\underline{N}^3$-MBI)], **2**, *cis,trans*-[Ru^{II}(CO)$_2$Cl$_2$($\underline{N}^3$-MBI)$_2$], **3**, and *fac*-[Ru^{II}(CO)$_3$Cl$_2$($\underline{N}^3$-DMBI)], **4**.

Vector	Length			
	2	**3A**	**3B**	**4**
Ru1-Cl1	2.4056(9)	2.399(2)		2.400(1)
Ru1-Cl2	2.4005(8)	2.403(2)		2.415(1)
Ru1-N3A	2.108(2)	2.125(4)	2.128(5)	2.105(2)
Ru1-C11	1.907(3)	1.868(7)	1.900(6)	1.891(4)
Ru1-C12	1.885(3)			1.887(4)
Ru1-C13	1.911(3)			1.931(4)
O1-C11	1.126(3)	1.119(6)		1.134(4)
O2-C12	1.132(3)	1.064(5)		1.136(4)
O3-C13	1.113(3)			1.111(4)
N3A-C2A	1.320(3)	1.370(6)	1.372(9)	1.324(4)
N1A-C2A	1.340(3)	1.307(6)	1.300(8)	1.335(4)
N3A-C9A	1.396(3)	1.355(7)	1.329(5)	1.399(4)
N1A-C8A	1.375(3)	1.430(7)	1.352(8)	1.372(4)
N1A-C10A	1.451(4)	1.435(7)	1.550(9)	
C9A-C4A	1.387(4)	1.355(7)	1.3900	1.392(5)
C4A-C5A	1.373(4)	1.398(7)	1.390	1.381(5)
C6A-C5A	1.389(4)	1.338(7)	1.390	1.401(5)
C7A-C6A	1.360(4)	1.432(8)	1.390	1.377(5)
C8A-C7A	1.397(3)	1.330(7)	1.390	1.377(5)
C9A-C8A	1.389(3)	1.414(7)	1.390	1.384(5)
C5A-C10A				1.546(5)
C6A-C10B				1.505(5)

Vectors	Angle			
	2	**3A**	**3B**	**4**
Cl2-Ru1-Cl1	91.75(3)	178.0(6)		89.3(3)
N3A-Ru1-Cl1	88.97(6)	86.6(1)	87.9(2)	88.8(1)
C11-Ru1-Cl1	85.76(9)	90.9(2)		87.6(1)
C12-Ru1-Cl1	178.40(9)	91.2(2)		179.7(1)
C13-Ru1-Cl1	87.34(11)			88.8(1)
N3A-Ru1-Cl2	87.92(6)	92.3(1)	90.3(1)	90.8(3)
C11-Ru1-Cl2	177.34(9)	90.9(2)		176.9(1)
C12-Ru1-Cl2	87.33(9)	89.2(2)		90.7(1)
C13-Ru1-Cl2	85.73(10)	87.2(2)		87.4(1)
C11-Ru1-N3A	91.09(10)	93.1(2)	177.8(2)	90.1(1)

C12-Ru1-N3A	92.29(10)	176.3(2)	89.8(2)	90.8(1)
C13-Ru1-N3A	172.55(11)			174.6(2)
C12-Ru1-C11	95.18(12)	89.9(2)		92.4(2)
C11-Ru1-C13	95.09(14)			92.6(2)
C12-Ru1-C13	91.30(14)			91.6(2)
C2A-N3A-Ru1	124.04(17)	123.6(4)	121.5(5)	123.4(2)
C9A-N3A-Ru1	129.97(17)	131.9(4)	132.7(4)	131.1(2)
O1-C11-Ru1	177.8(3)	176.6(5)		177.9(3)
O2-C12-Ru1	178.8(3)	177.3(5)		179.3(3)
O3-C13-Ru1	175.5(3)			175.7(4)
N3A-C2A-N1A	112.5(2)	113.0(6)	110.6(9)	111.9(3)
C2A-N3A-C9A	105.9(2)	104.2(5)	105.7(5)	105.4(3)
C4A-C9A-N3A	131.2(2)	130.7(6)	131.0(3)	131.6(3)
C8A-C9A-N3A	107.9(2)	112.0(6)	109.0(3)	108.6(3)
C5A-C4A-C9A	117.0(3)	118.0(6)	120	118.7(4)
C4A-C5A-C6A	121.7(3)	123.7(6)	120	120.7(4)
C7A-C6A-C5A	122.1(3)	119.6(6)	120	120.5(3)
C6A-C7A-C8A	116.6(3)	115.1(6)	120	118.4(3)
C9A-C8A-C7A	121.6(3)	126.2(6)	120	122.0(3)
N1A-C8A-C7A	131.7(3)	131.4(6)	133.9(4)	132.3(3)
N1A-C8A-C9A	106.7(2)	102.4(5)	105.9(4)	105.7(3)
C4A-C9A-C8A	120.9(2)	117.3(6)	120	119.8(3)
C2A-N1A-C8A	107.1(2)	108.4(5)	108.5(8)	108.3(3)
C2A-N1A-C10A	126.8(3)	126.0(6)	125.2(8)	
C8A-N1A-C10A	126.1(3)	125.6(5)	126.0(6)	
C4A-C5A-C10A				119.2(4)
C6A-C5A-C10A				120.1(3)
C5A-C6A-C10B				120.3(4)
C7A-C6A-C10B				119.3(4)

Details for Packing Forces for 2, 4 and 3

The selected *intra*-molecular and *inter*-molecular HBTIs for **2** are reported in **Figure S1a** and **Table S3**. The *intra*-molecular ones (for **2**) involve mainly the chlorido ligands as acceptors and the C2 atom at MBI ligand as donor. Even though the contact distances are relatively short, the angles at H2s are barely acceptable for HBTIs (*i.e.*, are far from idealized 180°: average 103.5(5)°).

The selected *inter*-molecular HBTIs for **2** have chlorido ligands and oxygen atoms from carbonyl ligands as acceptors and methyl, and imidazole (C2) or benzo (C4) atoms as donors. The contact donor…acceptor distances are as short as 3.125(4) Å (see O3…C4) or relatively long as 3.718(4) Å Cl2…C10). The short contacts correspond to narrow angles at H (Ĥ4, average 105 (1)°), whereas the long contacts are related to wide angles at H (Ĥ12A, 157(1)°). The structural parameters for the selected HBTIs for **4** are listed in **Table S3** and a drawing of *inter*-molecular interaction is reported in **Figure S1b.**

Planes for 2. The *endo*-cyclic atoms of the imidazole ring and benzo ring do not deviate significantly from coplanarity, whereas the metal atoms deviate by 0.101(1) Å from the imidazole plane. The "equatorial plane" defined by donors Cl1, Cl2, C11, C12 (max. deviation C11, 0.022(3) Å) contains the metal atom (dev 0.003(1) Å). The dihedral angle between equatorial plane and imidazole plane (*endo*-cyclic atoms) is 87.0(2)°. Selected $\pi…\pi$ stacking interactions are depicted in **Figure S2a,b**. The overlap between the planes is *ca.* 20% (MBI surface) and the contact distances are as short as N1A···C6(-x+1,-y+1,-z+2) (3.422(4) Å), C7A···C9 (3.440(4) Å) and C6A···C2 (3.467(5) Å).

Hydrogen bond HBI or hydrogen bond type HBTIs for 3. The HBTIs for the complex molecule **3** HBTIs are listed in **Table S3**. The shortest *intra* contacts between acceptor and donor are those labeled Cl1···C2A 3.246(8) Å, Ĥ2A 101.1(5)° and Cl1···C2B 3.273(8) Å, Ĥ2B 101.6(6)°. HBTI donated by C4 atoms have larger contacts but have more favorable angles at Hs.

Inter-molecular HBTIs are almost of the Cl…H-C and O…H-C fashion and relatively short donor acceptor contacts are Cl1···C5A(x,-y+3/2,z+1/2) 3.579(8) Å, Ĥ5A 133.0(6)° and O2···C10A(x,-y+3/2,z+1/2) 3.486(9) Å, Ĥ10A 108.6(4)° (**Figure S3** and **Table S3**).

Packing interactions for 3.The crystal packing interactions stabilize the crystal structure (**Figure S4** and **Figure S5**). Selected short *inter*-atomic contacts are N1A…C5A, 3.564(8) Å; C2A…C6A, 3.657(9) Å and C7A…C9A, 3.589(9) Å (the second atom of each couple is in position (-x+1,-y+2,-z+1). Thus, they are not very short (taking into account that the C…C contact distances for nucleobases in DNA might be as short as *ca.* 3.4 Å),[43] but one has to take into account that the overlap region for **3** is large and the benzimidazole rings are exactly parallel to each other.

Table S3. Selected *intra*-molecular and *inter*-molecular HBTIs for *fac*-[Ru^{II}(CO)$_3$Cl$_2$(*N^3*-MBI)], **2**, *cis,trans*-[Ru^{II}(CO)$_2$Cl$_2$(*N^3*-MBI)$_2$], **3**, and *fac*-[Ru^{II}(CO)$_3$Cl$_2$(*N^3*-DMBI)], **4**. The symmetry operations are also reported.

Acceptor…Donor	Length (Å)	Acceptor…Donor	Angle (°)
fac-[Ru^{II}(CO)$_3$Cl$_2$(*N^3*-MBI)], 2			
Intra-molecular			
Cl1···C2A	3.340(3)	Cl1···H2A-C2A	105(1)
Cl2···C2A	3.308(3)	Cl2···H2A-C2A	102(1)
O1···C4A	3.783(4)	O1···H4A-C4A	121(1)
Inter-molecular			
Cl2···C10A(-x,-y+1,-z+1)	3.718(4)	Cl2···H12A-C10A	157(1)
Cl2···C2A(-x,-y+1,-z+1)	3.673(3)	Cl2···H2A-C2A	143(1)
O3···C4A(x-1,-y+1/2+1,z-1/2)	3.125(4)	O3···H4A-C4A	106(1)
O3···C5A(x-1,-y+1/2+1,z-1/2)	3.251(5)	O3···H5A-C5A	103(1)
cis,trans-[Ru^{II}(CO)$_2$Cl$_2$(*N^3*-MBI)$_2$], 3			
Intra-molecular			
Cl1···C2A	3.246(8)	Cl1···H2A-C2A	101.1(5)
Cl1···C2B	3.273(8)	Cl1···H2B-C2B	101.6(6)
Cl2···C4A	3.567(7)	Cl2···H4A-C4A	123.8(4)
Cl2···C4B	3.426(8)	Cl2···H4B-C4B	124.8(6)
O1···C4A	3.548(8)	O1···H4A-C4A	119.7(7)
O2···C2B	3.697(8)	O1···H2B-C2B	110.3(6)
Inter-molecular			
Cl1···C10A(-x+1,y-1/2,-z+1/2)	3.790(6)	Cl1···H10A-C10A	138.0(6)
Cl1···C6A(-x+1,-y+2,-z+1)	3.671(8)	Cl1···H6A-C6A	139.2(6)
Cl1···C5A(x,-y+3/2,z+1/2)	3.579(8)	Cl1···H5A-C5A	133.0(6)
Cl1···C4A(x,-y+3/2,z+1/2)	3.675(8)	Cl1···H4A-C4A	120.4(5)
Cl2···C10B(-x+2,-y+1,-z+1)	3.84(1)	Cl2···H10B-C10B	143.9(5)
Cl2···C2A(x,-y+3/2,z+1/2)	3.804(8)	Cl2···H2A-C2A	143.2(6)
Cl2···C10A(x,-y+3/2,z+1/2)	3.885(7)	Cl2···H10A-C10A	124.7(6)
O1···C6A(-x+1,y-1/2,-z+3/2)	3.826(8)	Cl1···H6A-C6A	110.1(5)
O1···C5A(-x+1,y-1/2,-z+3/2)	3.484(9)	O1···H5A-C5A	144.2(6)
O1···C7A(-x+1,-y+2,-z+1)	3.518(9)	O1···H7A-C7A	149.2(6)
O1···C10A(x,-y+3/2,z+1/2)	3.793(8)	O1···H10A-C10A	151.0(6)
O2···C7B(-x+2,-y+1,-z+1)	3.47(1)	O2···H7B-C7B	130.4(5)
O2···C10A(x,-y+3/2,z+1/2)	3.486(9)	O2···H10A-C10A	108.6(4)
fac-[Ru^{II}(CO)$_3$Cl$_2$(*N^3*-DMBI)], 4			
Intra-molecular			
Cl2···C2A	3.220(4)	Cl2···H2A-C2A	107.3(3)

O2···C4A	3.701(6)	O2···H4A-C4A	120.8(4)
O1···C4A	3.632(6)	O1···H4A-C4A	121.5(4)
Inter-molecular			
Cl1···N1A(-x,y-1/2,-z+3/2)	3.292(5)	Cl1···H1A-N1A	128.7(6)
Cl2···N1A(-x,y-1/2,-z+3/2)	3.391(5)	Cl2···H1A-N1A	151.4(5)
O1···C10B(x,y-1,z)	3.497(6)	O1···H10B-C10B	133.1(6)
O2···C10A(x-1/2,-y+1/2,-z+1)	3.774(6)	O2···H10A-C10A	129.2(5)
O2···C10B(x-1/2,-y+1/2,-z+1)	3.333(6)	O2···H10B-C10B	148.9(6)
O3···C10B(x,y-1,z)	3.499(5)	O3···H10B-C10B	119.3(7)

(a)

(b)
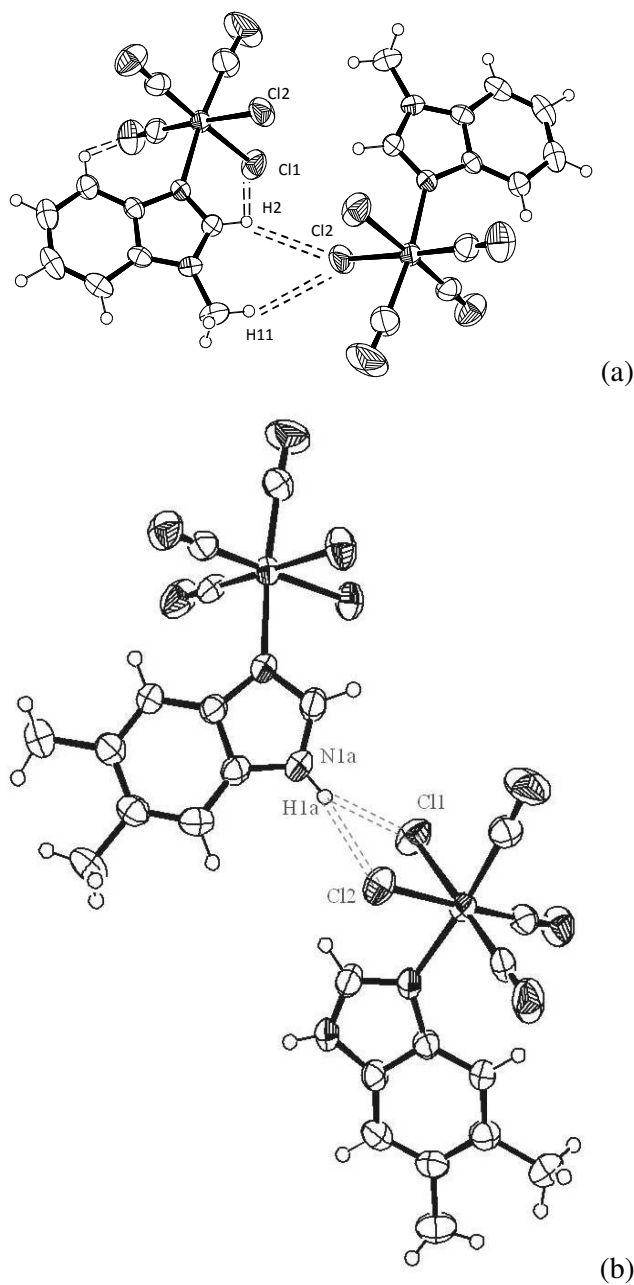
Figure S1. Diagram showing selected *intra-* and *inter*-molecular HBTIs (dashed lines) for (a) complex **2**: interactions between C–H…O (*intra*) and (MBI)C2–H(-x, -y+1, -z+1) and (MBI,Me)H (same molecule) to Cl2(Ru) (*inter*) are represented; (b) complex **4**: Cl1···H1A–N1A (3.292(8) Å, 129(1)°) and Cl2…H1A–N1A (3.391(8) Å, 151(1)°). Hydrogen atom H1A belongs to the molecule that lies in –x,y-1/2,-z+3/2.

(a)   (b)

(c)
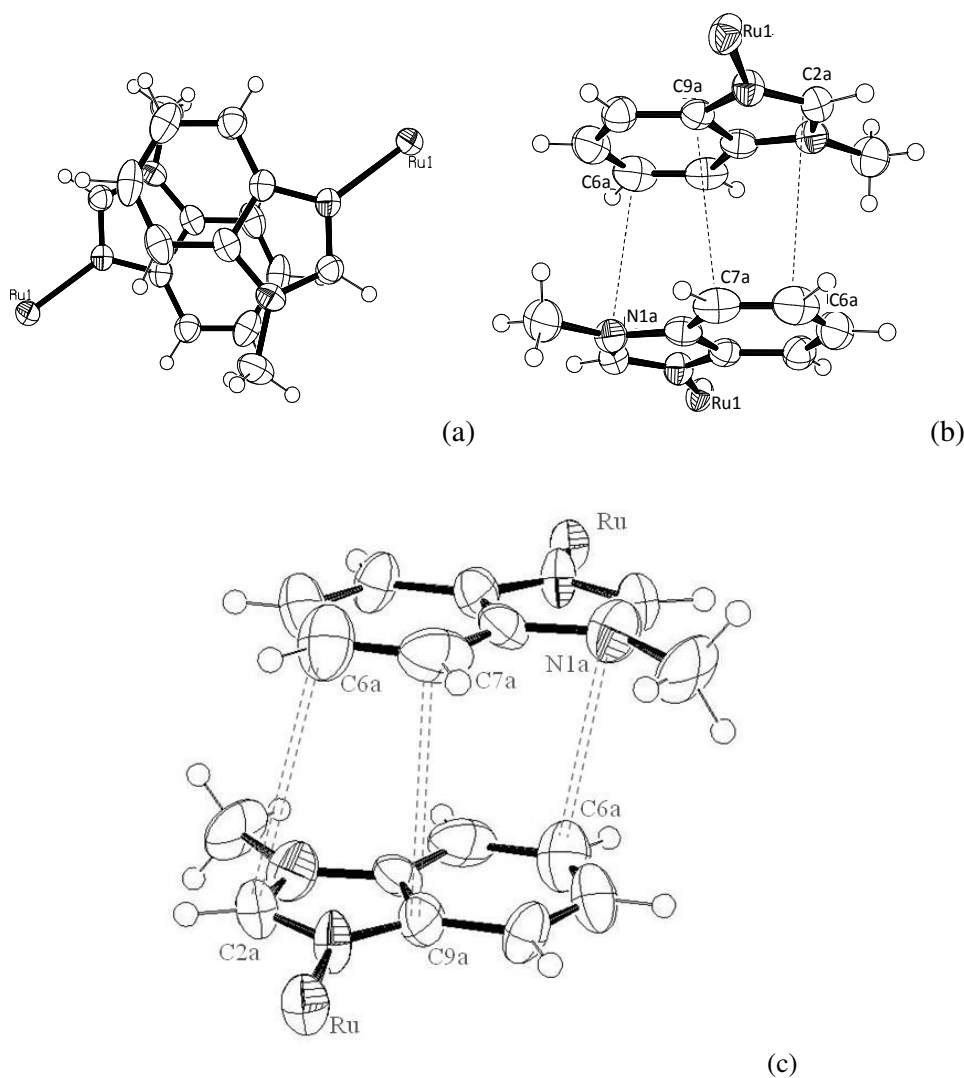
Figure S2. Stacking interactions for the crystal structure of **2**: (a) view along the normal to the plane of MBI; (b) view along a line that is *ca.* 70° with respect to the normal of the MBI plane. A view of the *inter*-molecular *stacking* interactions between two MBI moieties in the structure of **3** is represented in (c): it is almost parallel to the *stacked* planes.
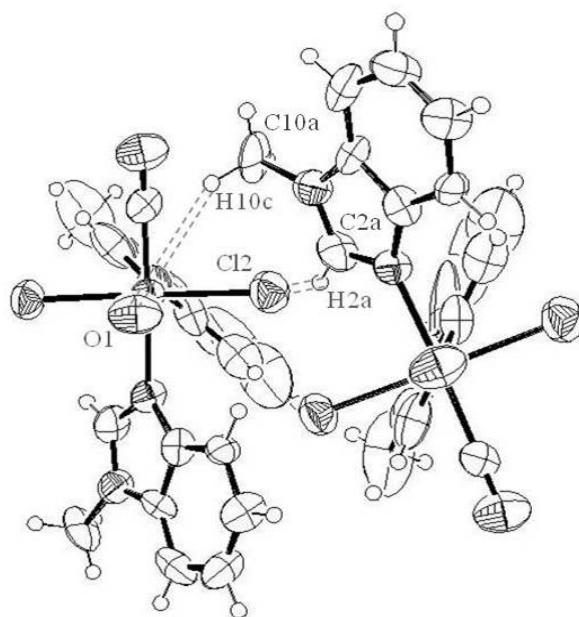
Figure S3. Selected *inter*-molecular hydrogen bonds Cl2…H2A–C2 (3.804(8)Å; 143.2(6)°) and O1…H10–C10 (3.793(8) Å; 151.0(6)°) for **3**. The Hs involved in the HBTIs belong to the molecule that lies at (x,-y+3/2,z+1/2).
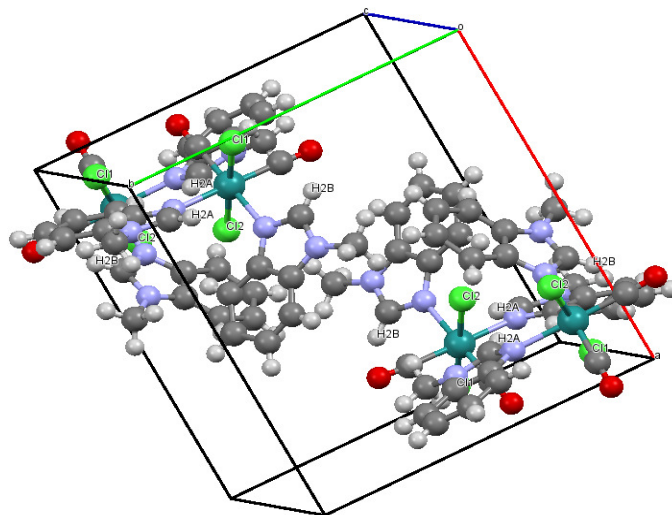
Figure S4. Diagram showing the content of the crystal cell for **3** almost along the **b** cell axis.
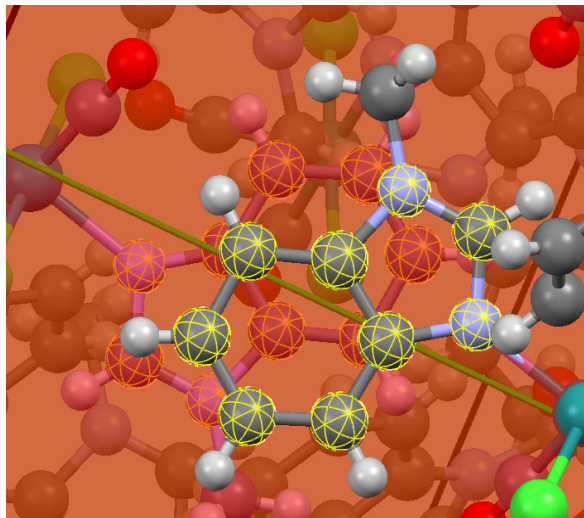
Figure S5. Diagram showing two *stacked* benzimidazole rings for **3** as viewed along the normal to the stacked planes, with the heavy atoms evidenced as reticulated balls. The view explicitly reveals that the overlapping region is vast; the two planes are rigorously parallel to each other. The lines that appear in green and brown colors represent the cell axes as they appear after zooming the cell.

Details on IR Spectroscopy

Infrared spectroscopy was used in order to investigate the spectra of the starting complexes **1** and **2** in the solid state, in anhydrous alcoholic and in hydro-alcoholic solutions to assess their stability/reactivity, as well as to investigate the spectra for **3** and **4** in the solid state.

The starting complex, *fac,anti*-[Ru^{II}(CO)$_3$Cl$_2$]$_2$, **1.** The ATR-FT IR spectrum for **1** in the solid state showed a sharp and intense peak at 2146 cm^{-1} (**Table S4** and **Figure S6**). In addition, a system of two relatively large and also intense peaks occurs in the region of 2100–2050 cm^{-1}. The spectrum is in agreement with that reported by Johnson et al.[46] The peaks are assignable to the stretching vibrations for the C≡O ligands being in agreement with computed values (this work) via DFT at the B3LYP/(Ru,Lanl2dz;CClO,6-31G**) level of theory (see below). The computed frequencies are at 2148, 2154 and 2207 cm^{-1} having intensities by 1157.697, 1014.362 and 943.586 km mol^{-1}, respectively. Computations allowed assigning the first computed peak to the vibrations of carbonyl functions that lie in the equatorial plane of the complex molecule, whereas the other two peaks to carbonyl ligands including those in axial positions. The computed frequencies are higher than the experimental ones and the correction factor, experimental/computed ratio being in the range 0.961–0.971, in good agreement with those reported by other authors.[46,47]

The spectrum of **1** in anhydrous methanol (13.67 mM, freshly prepared and after the subtraction of the signal for methanol, region 1900–2200 cm^{-1}) is reported in **Figure S7a**. It shows a sharp and medium intensity peak at 2130 cm^{-1} in agreement with the spectrum at solid state and the computed one, taking into account that in solution the bands undergo a red shift with respect to the solid state (especially the band at 1990 cm^{-1}). After an hour from the preparation of the solution, the spectrum did not change significantly (**Figure S7b**).

It was then decided to see if the addition of water had a significant influence. Relevant spectra for **1** in 90:10 v/v, after 10 min and 90 min from preparation, and then in methanol:water 50:50 v/v, and finally after the addition of NaOH (2 mg/mL) were collected and recorded (**Figure S7c–f**).

The data for studies in hydroalcoholic solutions for both **1** and **2** (and even in the presence of sodium hydroxide are in agreement with those reported previously for fac-$Ru^{II}(CO)_3$ core complexes,[48] and with the reaction sequence:

$$fac\text{-}[Ru^{II}(CO)_3L_3]^{2+} + OH^- \;\rightarrow\; [(HOOC)Ru^{II}(CO)_2L_3]^+ \;\rightarrow\; [HRu^{II}(CO)_2L_3]^+ + CO_2 \quad \text{(Eq. 1)}$$
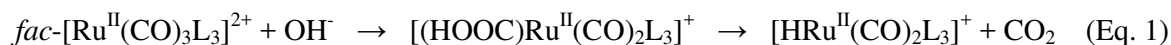
(where L may be H_2O) that brings about $Ru(CO)_2$ species and release of carbon dioxide.

Finally, the spectra at solid state for **3** and **4** are in agreement with other works.[42,49,50]

fac-$[Ru^{II}(CO)_3Cl_2(\underline{N}^3\text{-MBI})]$, **2**. The spectrum of **2** is represented in **Figure S8** and selected peaks are listed in **Table S3**. The bands relevant to the C≡O stretching vibrations occur at 2133, 2060 and 2037 cm^{-1}, showing red shifts by $ca.$ 10–30 cm^{-1} with respect to those found for **1**. That is probably related to a stronger donating effect by MBI when compared to CO and chlorido ligands. Another contribution can stem from the C4–H…π (O≡C) and steric interactions. The stretching of C2–H bond is recorded at 3119 cm^{-1} in agreement with corresponding values found for analogous compounds.[49]

The infrared spectrum of **2** in anhydrous methanol (0.1 mg/mL, the compound is less soluble than **1** in methanol, freshly prepared, in the region 1900–2200 cm^{-1}) is reported in **Figure S9a.** The peak at 2060 cm^{-1} is the most prominent in the region of carbonyl stretching and corresponds to the band at 2060 cm^{-1} in the spectrum of the solid compound **2**. Intensities of the bands at 2129 and 1980 cm^{-1} are much lower in solution than in the solid compound. After 24 h from preparation of the solution, some slight changes occurred (**Figure S9b**).

After that, the addition of water (50% v/v) was performed and significant changes occurred (**Figure S9c**). From those data, it is evident that the addition of water causes significant chemical reactions

which, in analogy with the study for **1** and in literature,[1,48] are assumed to be of the type described in the following Eq. S2:

$$\textit{fac-}[Ru^{II}(CO)_3Cl_2(\underline{N}^3\text{-MBI})] \; \xrightleftharpoons{H_2O} \; \textit{fac-}[Ru^{II}(CO)_3(H_2O)_3]^{2+} \; + \; 2Cl^- \; + \; MBI \quad (Eq.\ S2)$$

Then excess NaOH (0.5 mg/mL) was added to the hydroalcoholic solution of **2** (**Figure S9d**) showing that a phenomenon similar to that found for **1** should occur with shifts of bands relevant to carbonyl stretching vibrations towards red and attributable to reactions of the type reported in Eq. 1 (see above and see Santos et al.[48]). It has to be noticed that the evolution of CO_2 was inferred from the analogy of present infrared data (see above) and the work by others cited in Santos et al.,[48] but no direct measurements for the evolution of carbon dioxide and carbon monoxide was attempted in this work.

Dimer **1** and complex **2** were also investigated in MeOH/DMSO media. The IR spectrum for the dimer **1** in MeOH/DMSO (100:5, v/v; 20 °C) freshly prepared solution (5 min, **Figure S10a**) showed two main significant peaks in the C-O stretching vibration region (2060 and 2130 cm^{-1}) that compared well with the spectrum in pure MeOH. The spectrum of **1** in MeOH/DMSO showed an additional weaker peak at 2150 cm^{-1} that suggested that an initial reaction was occurring. After 1.5 h the pattern evolved towards two peaks (2060 and 2140 cm^{-1}, **Figure S10b**). This latter finding agreed with the initial formation of a species that, on the basis of literature, we attribute to [Ru(CO)$_3$Cl$_2$(DMSO)] (see also NMR in DMSO-d$_6$). The IR spectrum of freshly prepared solution of complex **2** dissolved in MeOH/DMSO (100:5, v/v; 20 °C, 5 min, **Figure S11a**) showed two peaks at 2045 and 2060 cm^{-1} and two less intense peaks at 2133 and 2165 cm^{-1}, in agreement with the spectrum in MeOH. Upon time elapsing (1.5 h, **Figure S11b**), the general pattern of peaks did not change much, but the shape of the couple of peaks around 2045 and 2060 cm^{-1}. That can be explained by the initial occurrence of displacement of reaction of MBI by DMSO (see also NMR in DMSO-d$_6$).

cis,trans-[Ru^{II}(CO)$_2$Cl$_2$(*N*^{3}-MBI)$_2$], **3**. The spectrum of **3** is reported in **Figure S12**, whereas the values of the most relevant frequencies are listed in **Table S3**. All frequencies corresponding to the C≡O bonds undergo red shifts with respect to those for **1**, in agreement with a weakening of the C≡O bond due to larger sigma donation by MBIs (*trans* to CO) when compared to that by chlorido ligands.[50] The spectrum of **3** has two bands relevant to the stretching of C≡O bonds owing to the higher symmetry of the Ru^{II}(CO)$_2$ moiety of **3** compared to that of Ru^{II}(CO)$_3$ for **2** and **4**.

fac-[Ru^{II}(CO)$_3$Cl$_2$(*N*^{3}-DMBI)], **4**. The spectrum of **4** is reported in **Figure S13**, whereas the values of the frequencies for the selected bands are reported in **Table S3**. When the values are compared to those for the starting dimer complex *fac,anti*-[Ru^{II}(CO)$_3$Cl$_2$]$_2$, **1**, a red shift for the stretching C≡O bands is evident, which is due to the stronger donation by DMBI compared to chlorido ligands, increasing the electronic charge on Ru^{II}, allowing a stronger back donation to the carbonyl ligands and, thus, weakening the C≡O bond force constant.[50] The sharp and medium to intense band at 3284 cm^{-1} is assignable to the C2–H bond stretching motion, whereas the effect for the N–H stretching is probably ascribable to the shoulder at *ca.* 3600–3400 cm^{-1} [42] because of the *inter*-molecular HBTIs that involve the N1–H…Cl(Ru) functions.

Table S4. Selected experimental IR bands (cm^{-1}) for starting dimeric complex *fac,anti-*[Ru^{II}(CO)$_3$Cl$_2$]$_2$, **1** (CORM2), *fac*-[Ru^{II}(CO)$_3$Cl$_2$($\underline{N}^3$-MBI)], **2**, *cis,trans*-[Ru(CO)$_2$Cl$_2$($\underline{N}^3$-MBI)$_2$], **3**, and *fac*-[Ru^{II}(CO)$_3$Cl$_2$($\underline{N}^3$-DMBI)], **4**, recorded from KBr matrix. The relative intensities of the IR absorption bands are labeled through the qualitative symbols s (strong), m (medium) and w (weak).

Stretching	1	2	3	4
(Ru) C≡O	2146 (s)	2133 (s)	2059 (s)	2133 (s)
(Ru) C≡O	2091 (s)	2060 (s)	1992 (s)	2074 (s)
(Ru) C≡O	2068 (s)	2037 (s)		2052 (s)
(benzo)C-H		3119 (m)	3114 (w)	3152 (m)
(imidazole)C2-H				3284 (s)
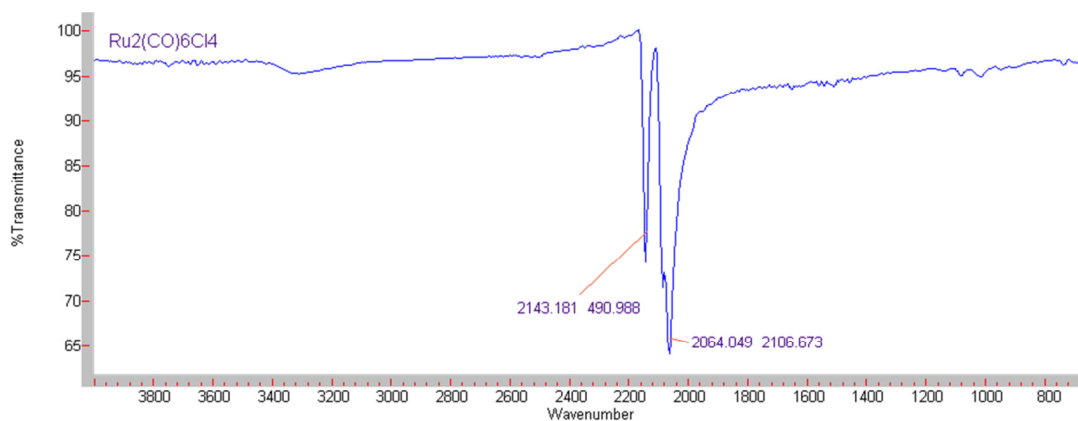
Figure S6. ATR-FTIR spectrum of *fac,anti*-[Ru^{II}$_2$(CO)$_6$Cl$_4$], **1**, CORM2, solid state, fine powder (25 °C).
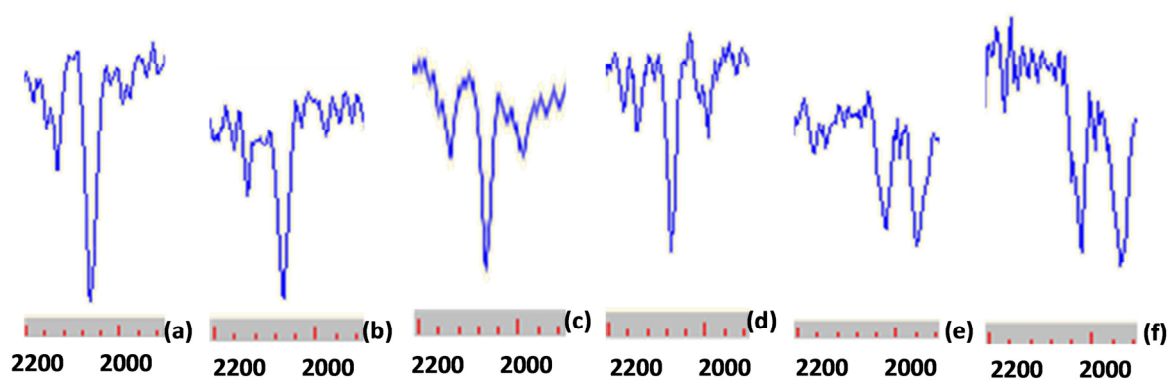
Figure S7. ATR-FTIR spectrum of *fac,anti*-[Ru$^{II}_2$(CO)$_6$Cl$_4$], **1**, CORM2, in anhydrous methanol after the subtraction of the solvent in the spectral region 2200–1900 cm^{-1}, (a) fresh solution; (b) after 60 min; (c) in methanol:water 90:10 v/v, freshly prepared; (d) in methanol:water 50:50 v/v, after 60 min; (e) in methanol:water 50:50 v/v, after 60 min from the preparation of the solution and after the addition of NaOH (2 mg/mL); (f) after 24 h at 23 °C.
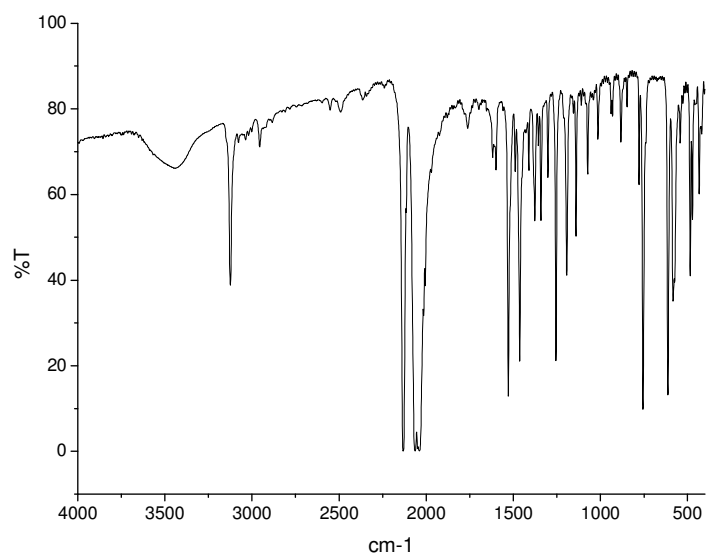
Figure S8. FT-IR spectrum of *fac,cis*-[Ru(CO)$_3$Cl$_2$($\underline{N}^3$-MBI)], **2**, in KBr matrix (25 °C).
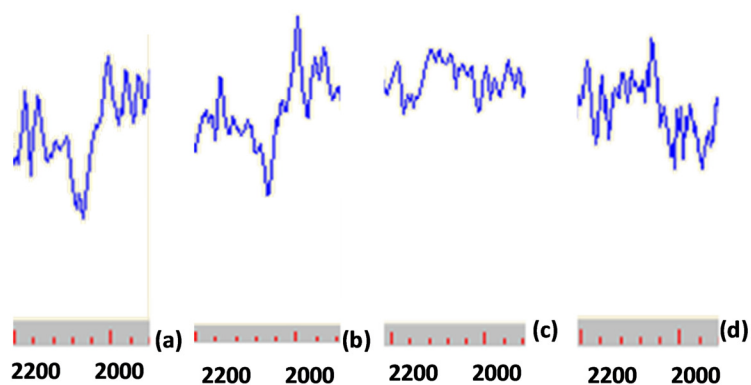
Figure S9. ATR-FTIR spectrum of *fac*-[Ru(CO)$_3$Cl$_2$($\underline{N}^3$-MBI)], **2**, in anhydrous methanol, after the subtraction of the solvent in the spectral region 2200–1900 cm^{-1}, (a) freshly prepared, (b) idem after *ca.* 24 h from the preparation of the solution; (c) spectrum for **2** in methanol:water 50:50 v/; (d) spectrum for **2** in methanol:water 50:50 v/v, after the addition of NaOH (0.5 mg/mL).

Figure S10. ATR-FTIR spectra for (a) a freshly prepared solution (5 min from mixing, 20 °C) of *fac*-[Ru$_2$(CO)$_6$Cl$_4$], **1**, CORM2, (6.8 mg) in 1 mL CH$_3$OH+50 µL DMSO; and (b) same as (a) but after 90 min from mixing. The IR region is between 1960 and 2240 cm^{-1} for both spectra.
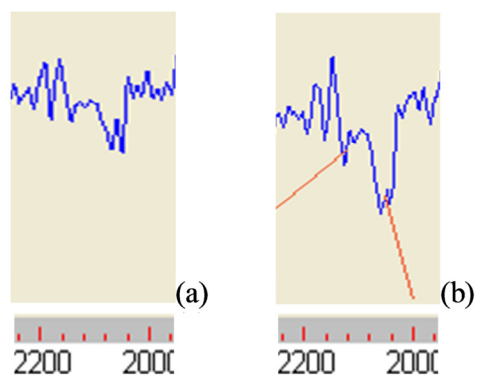
Figure S11. ATR-FTIR spectra for (a) a freshly prepared solution (5 min from mixing, 20 °C) of *fac*-[Ru(CO)$_3$Cl$_2$($\underline{N}^3$-MBI)], **2** (6.2 mg) in 1 mL CH$_3$OH + 50 µL DMSO; and (b) same as (a) but after 90 min from mixing. The IR region is between 1960 and 2240 cm^{-1} for both spectra. Red lines in (b) show peak maxima at 20161 and 2130 cm^{-1}, respectively.
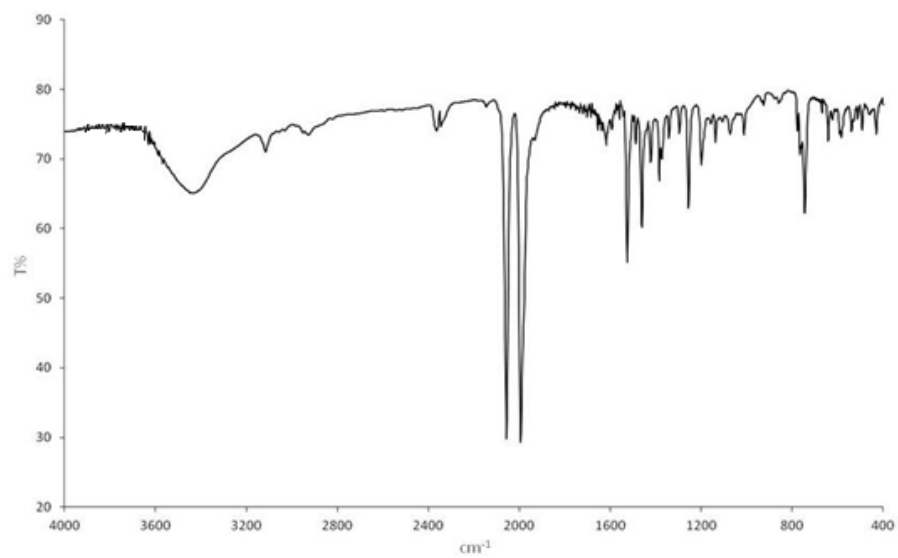
Figure S12. Infrared spectrum of *fac,cis*-[Ru^{II}(CO)$_2$Cl$_2$($\underline{N}^3$-MBI)$_2$], **3**, in KBr matrix.
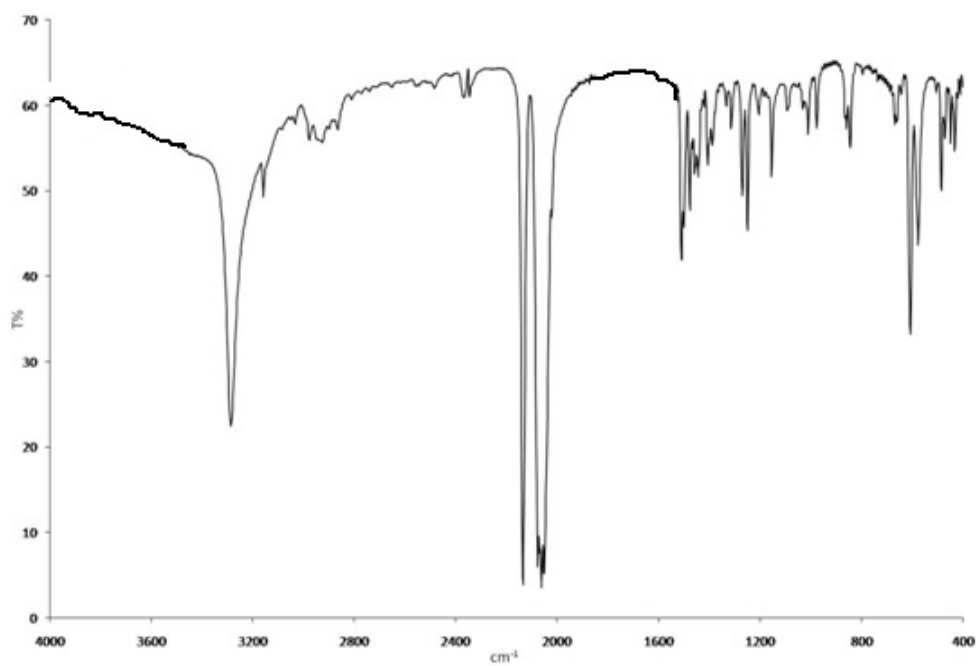
Figure S13. Infrared spectrum of *fac,cis*-[Ru^{II}(CO)$_3$Cl$_2$($\underline{N}^3$-DMBI)], **4**, in KBr matrix.

Details on NMR Spectroscopy
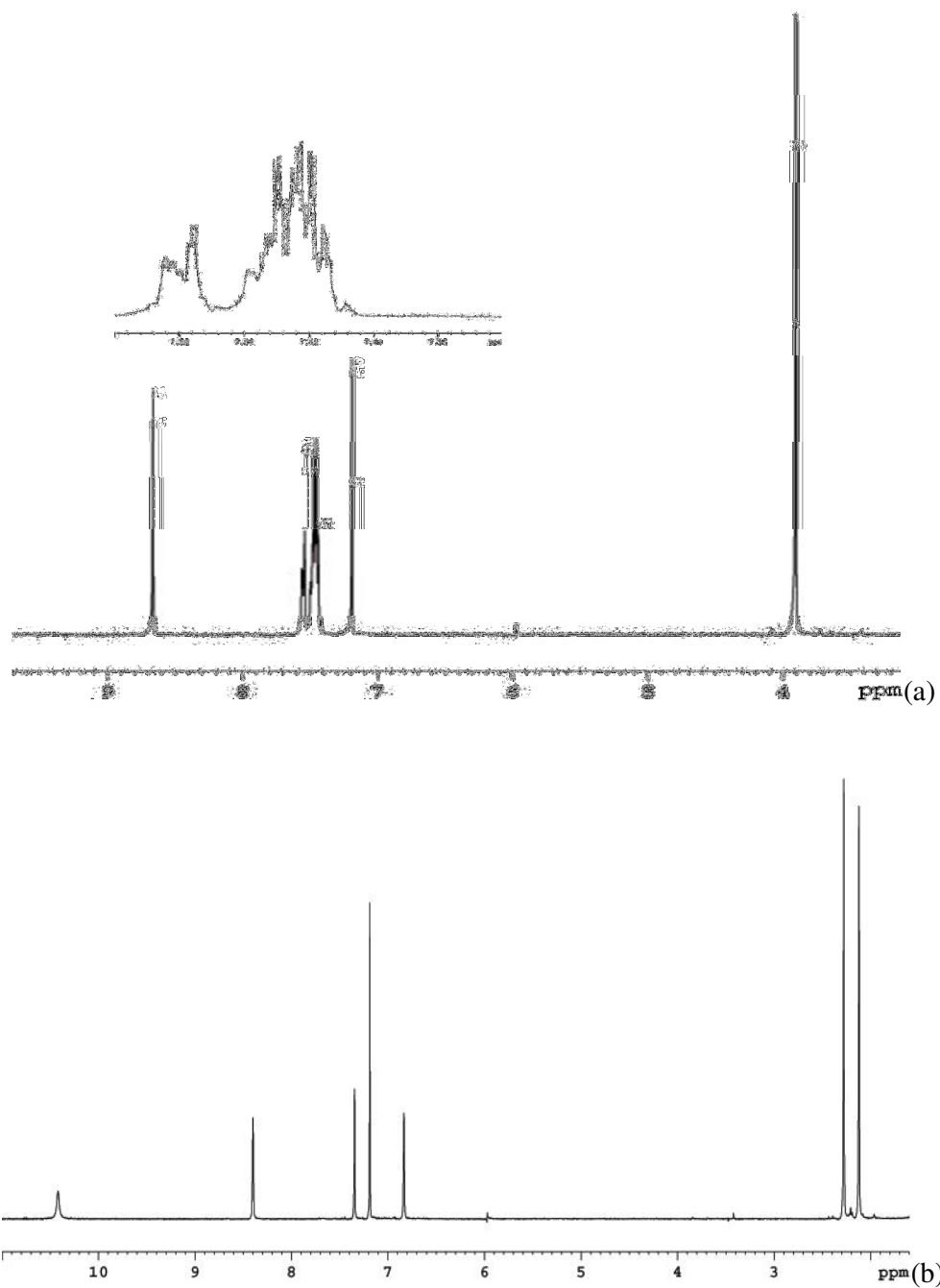
Figure S14. ^{1}H NMR spectra of (a) *fac*-[Ru(CO)$_3$Cl$_2$($\underline{N}^3$-MBI)], **2** and (b) *fac*-[Ru(CO)$_3$Cl$_2$($\underline{N}^3$-DMBI)], **4**, as dissolved in CDCl$_3$.
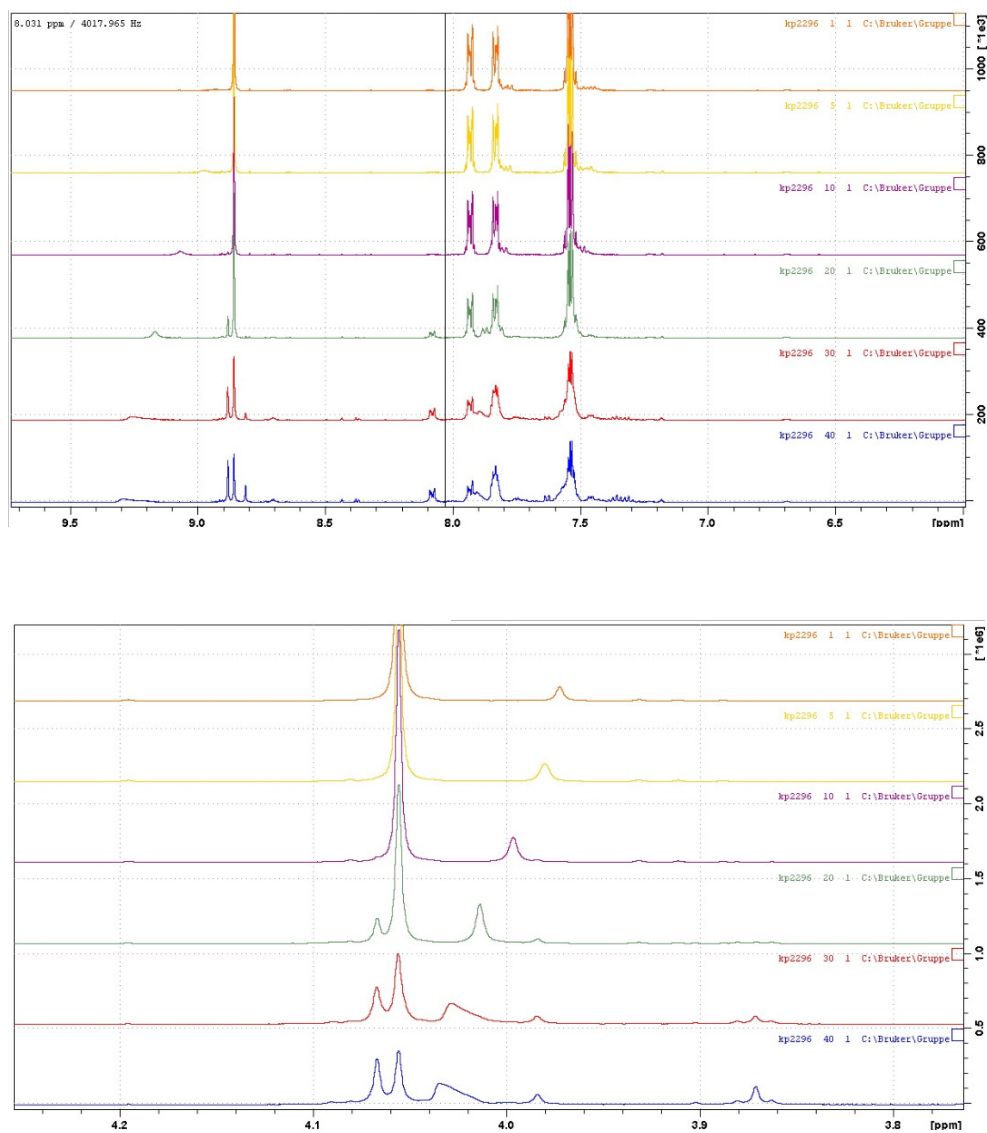
Figures S15. Different regions of ^{1}H NMR spectra of *fac*-[Ru(CO)$_3$Cl$_2$($\underline{N}^3$-MBI)], **2**, as dissolved in DMSO-D$_6$, upon time. From top to bottom the times of data collections from mixing **2** and DMSO-D$_6$ were: 1 min, 5 min, 10 min, 35 min, 120 min, 240 min.
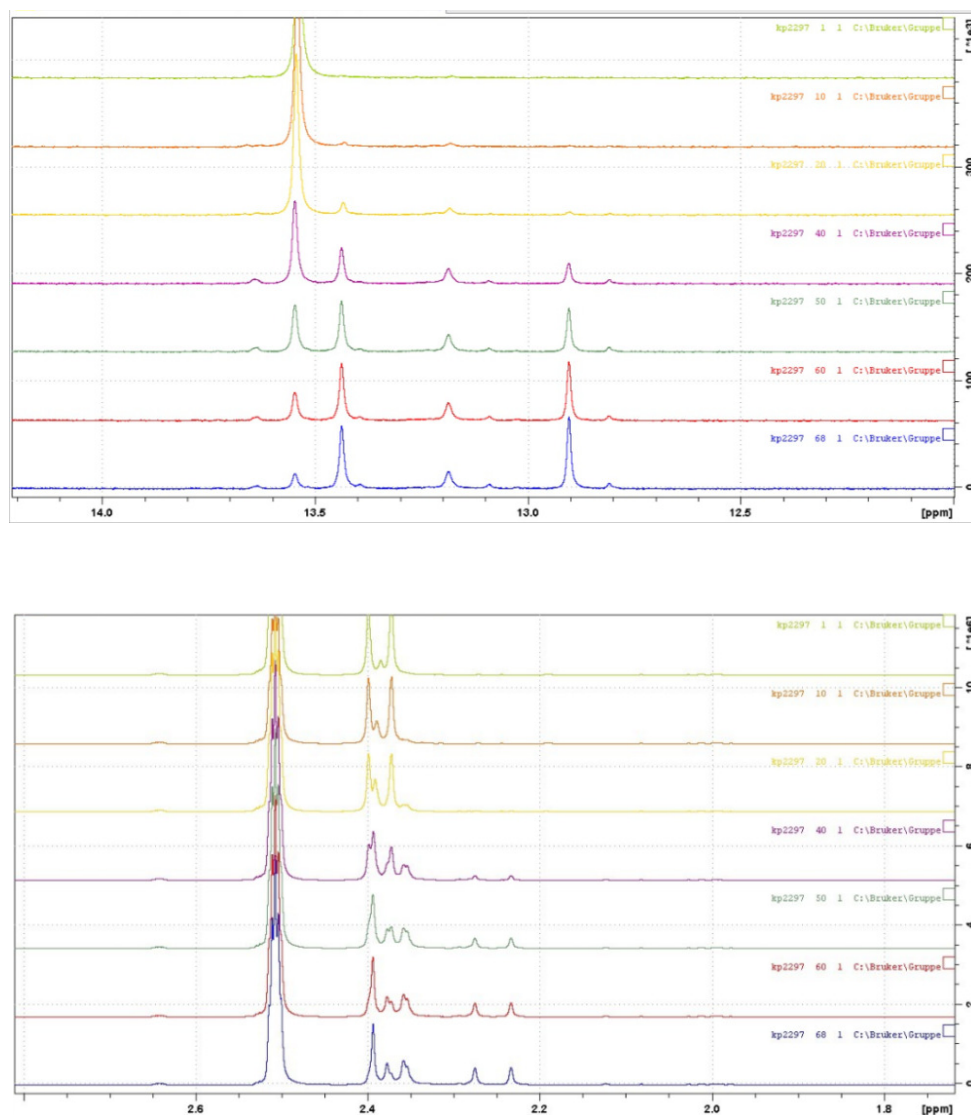
Figure S16. Different regions of ^{1}H NMR spectra of *fac*-[Ru(CO)$_3$Cl$_2$(*$\underline{N}^3$*-DMBI)], **4**, as dissolved in DMSO-D$_6$, upon time. From top to bottom the times of data collections from mixing **4** and DMSO-D$_6$ were: 1 min, 14 min, 45 min, 263 min, 556 min, 870 min, 1330 min.
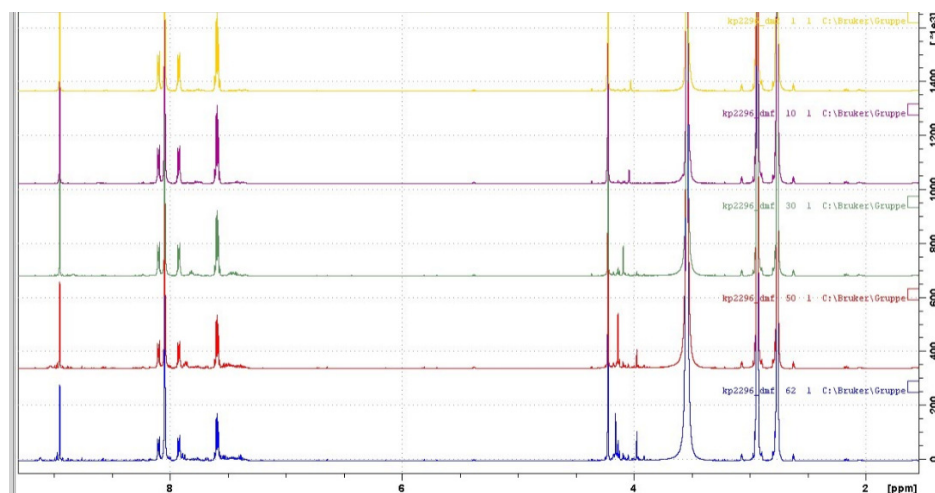
Figure S17. Different regions of ^{1}H NMR spectra of *fac*-[Ru(CO)$_3$Cl$_2$($\underline{N}^3$-MBI)], **2**, as dissolved in DMF-D$_7$, upon time. From top to bottom the times of data collections from mixing **2** and DMF-D$_7$ were: 1 min, 15 min, 90 min, 570 min, 995 min.

Figure S18. Different regions of ^{1}H NMR spectra of *fac*-[Ru(CO)$_3$Cl$_2$($\underline{N}^3$-DMBI)], **4**, as dissolved in DMF-D$_7$, upon time. From top to bottom the times of data collections from mixing **4** and DMF-D$_7$ were: 1 min, 14 min, 31 min, 150 min, 263 min, 497 min, 870 min, 1024 min.
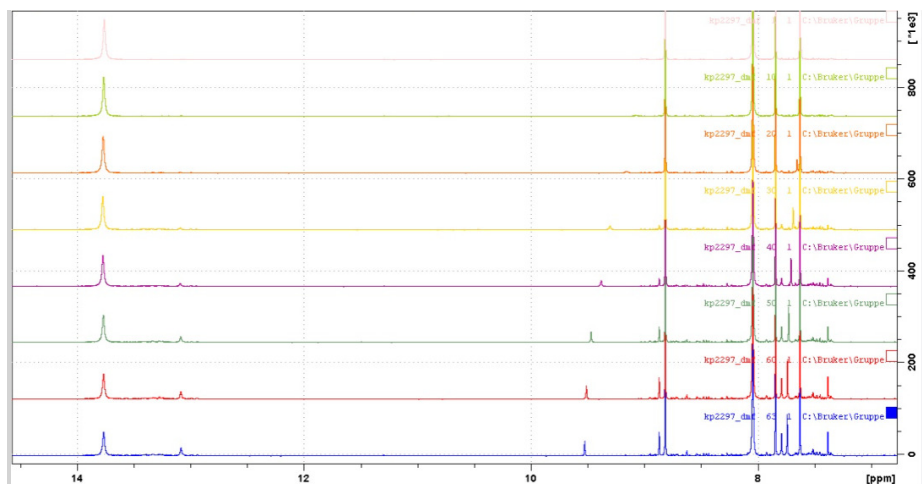
Details on HPLC
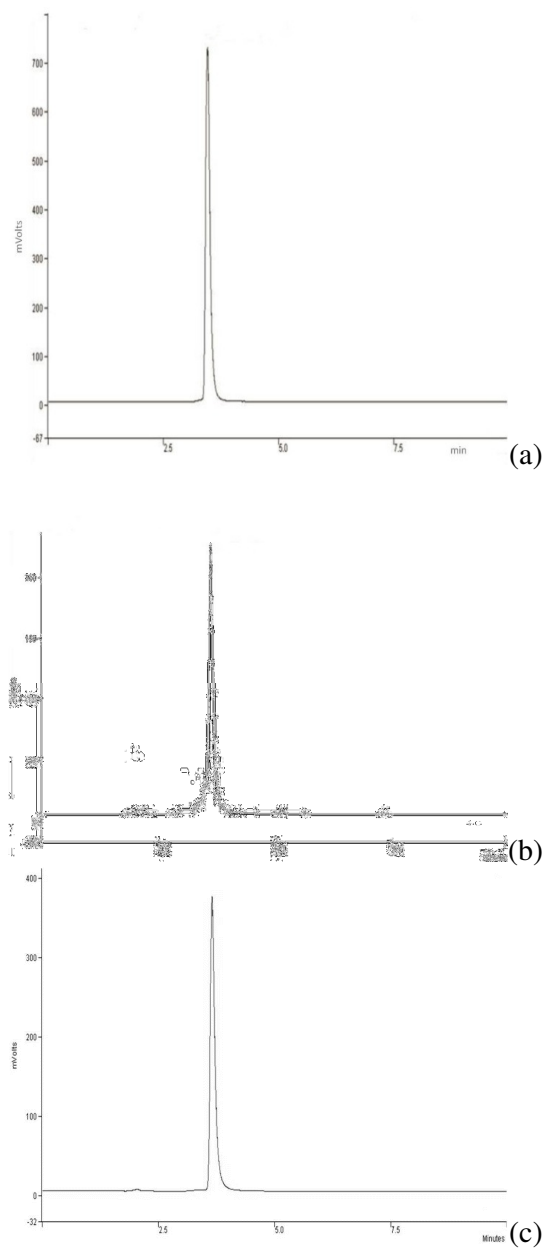
Figure S19. HPLC chromatogram for: (a) *fac*-[Ru^{II}(CO)$_3$Cl$_2$($\underline{N}^3$-MBI)], **2**; (b) *cis,trans*-[Ru^{II}(CO)$_2$Cl$_2$($\underline{N}^3$-MBI)$_2$], **3**; (c) *fac*-[Ru^{II}(CO)$_3$Cl$_2$($\underline{N}^3$-DMBI)], **4**, inCH$_3$CN and eluting with CH$_3$CN. Respective retention times 3.48, 3.61 and 3.65 min.

Details on Computations

DFT. The free ligands were computed at BS1, BS2, and BS3 levels of theory. Optimized structures are reported in **Figure 20a–c** and selected bond distances and angles are listed in **Table S5**. The computed structures for *fac,anti*-[Ru$^{II}_2$(CO)$_6$Cl$_4$] and *fac,syn*-[Ru$^{II}_2$(CO)$_6$Cl$_4$] and for the complexes *fac*-[Ru^{II}(CO)$_3$Cl$_2$(L)] (L = BIM, benzimidazole as model of DMBI; and MBI) were also computed at BS3 (and even at BS1 and BS2 levels of theory for selected conformations).

The computed enthalpy of formation at 298.15 K for the isomer *fac,anti*-[Ru$^{II}_2$(CO)$_6$Cl$_4$] is *ca.* 6.5 kcal/mol more favorable than that for *fac,syn*-[Ru$^{II}_2$(CO)$_6$Cl$_4$], confirming that the material described by other authors[46] and used as starting material in the present work is the *fac,anti* isomer (see **Figure S20a** for computed structure and **Table S5** for selected structural parameters).

The dimeric molecule *fac,anti*-[Ru$^{II}_2$(CO)$_6$Cl$_4$] was also preliminarily investigated regarding the reactivity with a water molecule and with a hydroxide anion in the gas phase. On optimizing an adduct that consisted of [Ru$^{II}_2$(CO)$_6$Cl$_4$]…H$_2$O (where the water molecule was set arbitrarily in a position such to donate an hydrogen to a terminal chlorido and to donate a second hydrogen to a bridging chlorido ligand), the adduct went to full convergence as represented in **Figure 4a**.

The hydrogen bond scheme with two O–H…Cl HBTIs was maintained, the O…Cl(bridging,b) and O…Cl(terminal,t) distances were 3.377 and 3.462 Å and Ĥ 118.2 and 161.2°, respectively. The effects on structural parameters for the dimer are small: a lengthening on one of the Ru–Clt by 0.016 Å, and on two of the Ru–Clb by 0.010 Å, and a corresponding shortening on the other two Ru–Clb by 0.006 Å. Noteworthy, these changes are in agreement with a breakage of the dimer, bringing about free chloride and a *fac*-{*Ru^{II}(CO)$_3$Cl$_2$} residue that is ready to link a nucleophile fragment (L) and produce *fac*-[Ru^{II}(CO)$_3$Cl$_2$(L)]. A second residue of the type *fac*-{**Ru^{II}(CO)$_3$Cl} can reasonably come out. This latter is ready to link two nucleophile fragments (2L or L and Cl⁻), resulting in *fac*-[Ru^{II}(CO)$_3$-Cl$_2$(L) or -Cl(L)$_2$] (charge has been omitted for the last hypothesis). The

effects on structural parameters for the dimer are small: a lengthening on one of the Ru–Clt by 0.016 Å, and on two of the Ru–Clb by 0.010 Å, and a corresponding shortening on the other two Ru–Clb by 0.006 Å. Noteworthy, these changes are in agreement with a breakage of the dimer, bringing about free chloride and a *fac*-{*Ru^{II}(CO)$_3$Cl$_2$} residue that is ready to link a nucleophile fragment (L) and produce *fac*-[Ru^{II}(CO)$_3$Cl$_2$(L)]. A second residue of the type *fac*-{**Ru^{II}(CO)$_3$Cl} can reasonably come out. This latter is ready to link two nucleophile fragments (2L or L and Cl$^-$), resulting in *fac*-[Ru^{II}(CO)$_3$-Cl$_2$(L) or -Cl(L)$_2$] (charge has been omitted for the last hypothesis). A subsequent computation towards preliminary theoretical investigation of the reactivity of *fac,anti*-[Ru$^{II}_2$(CO)$_6$Cl$_4$] with a hydroxide anion was performed, and a structure that had the OH$^-$ donating to a Clb (O…Cl 2.568 Å, Ĥ 119.0°) was optimized. Interestingly, the final structure (**Figure 4b**) had changed to a *fac*-[Ru^{II}(CO)$_2$(η^1-*C*-COOH)Cl(μ-Cl)$_2$Ru^{II}(CO)$_3$Cl]$^-$ anionic complex molecule. The Ru–C(COOH) bond distance (2.077Å) is much longer than the other two Ru–C bonds at the same metal (average 1.884Å) and even than the other three Ru–C bonds at the second metal center (average 1.927Å), in agreement with a protonated formato ligand. This latter donates a hydrogen to the terminal chlorido ligand, O…Cl 3.033 Å, Ĥ 151.9°, thus stabilizing a *cis,cis*-{Ru^{II}(CO)$_2$(η^1-*C*-COOH)Cl}$^-$, **F1**, fragment. This latter interacts with the other coordination entity via two chlorido bridges (see **Figure 4b** for selected bond lengths). Noteworthy, the Ru(**F1**)–Clb bond distances are 2.571 Å and 2.762 Å, whereas the other Ru–Clb bond lengths are 2.474 and 2.492 Å and the Ru…Ru contact distance is 3.822 Å. These data suggest that the dimer entity is on the way to break, and a coordinatively unsaturated particle *cis,cis*-{**Ru^{II}(CO)$_2$(η^1-*C*-COOH)Cl}$^-$ is a possible product. This is reminiscent of the particle type [(HOOC)Ru^{II}(CO)$_2$L$_3$]$^+$ invoked in Johnson et al.[46] and just above discussed in the analysis of IR data. Summarizing, these DFT computations confirm the hypothesis previously reported by others and in this work on the fate of *fac,anti*-[Ru$^{II}_2$(CO)$_6$Cl$_4$] and *fac*-[Ru^{II}(CO)$_3$Cl$_2$(L)] species when treated with water and/or hydroxide.

Fully optimized structures for *fac*-[Ru^{II}(CO)$_3$Cl$_2$(*$\underline{N}^3$*-MBI)] and *fac*-[Ru^{II}(CO)$_3$Cl$_2$(*$\underline{N}^3$*-BIM)] are depicted in **Figure 5** and selected structural parameters are listed in **Table 3** (and **Table S6**).

The conformation around the Ru–N(BIM) vector is staggered with respect to the two Ru–Cl bonds, and the projection of the heterocyclic base on the equatorial coordination plane is type-A (**Scheme 3**). The computed Ru–C(trans to N) and Ru–C(trans to Cl) are 1.944 and 1.932 Å, respectively, whereas experimental values for **4** are 1.931(3) and 1.889(3) Å, in agreement with the computed values and trend. Computed C–O(tN) and C–O(tCl) are 1.133 and 1.137 Å, respectively, and experimental corresponding values are 1.111(4) and 1.135(4) Å.

Interestingly, C–O vibrations cause computed absorption effects at 2189 cm^{-1} (527 km/mol), experimental 2133 cm^{-1} strong, that is mostly ascribable to CO(tN), and at 2130 cm^{-1} (588 km/mol) and 2106 cm^{-1} (700 km/mol), experimental strong effects occur at 2063 and 2029 cm^{-1}. The experimental over computed frequency ratios are in the acceptable range 0.974–0.995. Finally, the computed values for the more intense (albeit weak) effects related to Ru–Cl vibrations occur at 287 cm^{-1} (25 km/mol) and 318 cm^{-1} (20 km/mol); and computed absorptions for C–H and N–H at imidazole occur at 3277 cm^{-1} (27 km/mol) and 3653 cm^{-1} (119 km/mol).

As regards energy, the type-A conformer for the BIM derivative resulted to be the most stable, with type-B and -C being more unstable by 2.89 and 5.15 kcal/mol. Therefore, at 25 °C and in case just a thermal distribution based on free rotation around the Ru–N vector is assumed, the type-A conformer would be almost 99%, whereas type-B is negligible for *fac*-[Ru^{II}(CO)$_3$Cl$_2$(L)], and L = BIM and MBI. As regards L = DMBI, the presence of the type-B and -C conformers would be even less abundant because of the possible larger steric hindrance brought about by the methyl substituents on the benzo moiety.

Semiempirical. The structures for complexes *fac*-[Ru^{II}(CO)$_3$Cl$_2$(*$\underline{N}^3$*-BIM)] and *fac*-[Ru^{II}(CO)$_3$Cl$_2$(*$\underline{N}^3$*-MBI)] were optimized even at the semiempirical level ZINDO/1 (see **Figure S21a,b**). For both complexes, the type-A conformer was the most stable (by *ca.* 5 and 7 kcal/mol

when compared to type-B and type-C, respectively), in agreement with the findings from DFT. The structural parameters are acceptable and also in agreement with higher levels of theory and with experiments. The HOMO and LUMO orbitals for some of the conformers are represented in **Figure S21c-f**. From this latter figure, it is evident that both derivatives have HOMOs consisting of atomic orbitals from all the atoms of the molecules. Instead, LUMOs are composed by atomic orbitals from Ru, carbonyl and chlorido ligands. In other words, the excitations from HOMO to LUMO transfer electronic charge from the benzimidazole moiety into the metal and to CO and Cl$^-$ ligands. The trend for type-B and type-C conformers is the same as that for type-A.

Table S5. Selected structural parameters for ligands as computed via DFT methods at [BS2] and {BS3} level of theory; and for *fac,anti*-[Ru$_2^{II}$(CO)$_6$Cl$_4$], **1** (CORM2) and *fac,syn*-[Ru$_2^{II}$(CO)$_6$Cl$_4$] at [BS2] level. The subscripts are: t = terminal, b = bridging, eq = equatorial, ax = axial.

Length (Å) Angle (°)	MBI	BIM	IM	CO
N1-C2	[1.308] {1.306}	[1.307] {1.304}	[1.316] {1.313 }	
C2-N3	[1.378] {1.377}	[1.377] {1.377}	[1.366] {1.366}	
N1-C2-N3	[114.40] {114.16}	[113.72] {113.46}	[111.78] {111.53}	
C1-O1				[1.138] {1.128}

	fac,anti-[Ru$_2^{II}$(CO)$_6$Cl$_4$]	*fac,syn*-[Ru$_2^{II}$(CO)$_6$Cl$_4$]
Ru-Clt	[2.423]	[2.414]
Ru-Clb	[2.511]	[2.524]
Ru-C(*trans*Cl)	[1.961]	[1.949]
Ru-C(*cis*Cl)	[1.918]	[1.919]
Ru…Ru	[3.698]	[3.762]
Ru-Cl-Ru	[94.8]	[96.3]
Clt-Ru-Clb	[89.6]	[91.4]
Clt-Ru-C(*trans*)	[177.9]	[179.9]
Clt-Ru-C(*cis*)	[86.4]	[84.6]
Clb-Ru-C(*trans*)	[174.5]	[173.8]
Clb-Ru-C(*cis*)	[88.8]	[91.7]
Ceq-Ru-Ceq	[92.6]	[92.5]
Ceq-Ru-Cax	[95.0]	[95.5]

Table S6. Structural parameters (lengths, Å; angles, °) for the selected conformers of *fac*-[Ru^{II}(CO)$_3$Cl$_2$($\underline{N}^3$-MBI)] and *fac*-[Ru^{II}(CO)$_3$Cl$_2$($\underline{N}^3$-BIM)]. Values obtained from computations at (BS1), [BS2], and {BS3} levels of theory.

Parameters	[Ru^{II}(CO)$_3$Cl$_2$($\underline{N}^3$-MBI)]			[Ru^{II}(CO)$_3$Cl$_2$($\underline{N}^3$-BIM)]		
	Type A	Type B	Type C	Type A	Type B	Type C
Eel/ Hartrees	(-883.00373)	---	---	(-843.69930)	---	---
	[-883.35120]	---	---	[-884.02997]	---	---
	{-883.39443}	{-883.38981}	{-883.38599}	{-844.07250}	{-844.06790}	{-844.06429}
Distance/ Å						
Ru-Cl1	(2.491) [2.453] {2.456}	{2.446}	{2.455}	(2.490) [2.451] {2.454}	{2.445}	{2.455}
Ru-Cl2	(2.491) [2.453] {2.456}	{2.464}	{2.455}	(2.490) [2.451] {2.454}	{2.464}	{2.455}
Ru-C12(*trans* Cl1)	(1.916) [1.931] {1.932}	{1.932}	{1.929}	(1.917) [1.931] {1.932}	{1.933}	{1.930}
Ru-C11(*trans* Cl2)	(1.916) [1.931] {1.932}	{1.927}	{1.929}	(1.917) [1.931] {1.932}	{1.927}	{1.930}
Ru-C13(*trans* N3)	(1.937) [1.943] {1.944}	{1.942}	{1.940}	(1.936) [1.942] {1.944}	{1.941}	{1.939}
Ru-N3	(2.118) [2.150] {2.159}	{2.180}	{2.188}	(2.119) [2.153] {2.162}	{2.183}	{2.192}
N3-C2	(1.340) [1.321] {1.320}	{1.320}	{1.320}	(1.337) [1.319] {1.318}	{1.318}	{1.317}
C2-N1	(1.369) [1.353] {1.353}	{1.353}	{1.354}	(1.370) [1.354] {1.354}	{1.354}	{1.355}

C12-O2	(1.171) [1.143] {1.137}	{1.138}	{1.138}	(1.171) [1.143] {1.137}	{1.138}	{1.138}
C11-O1	(1.171) [1.143] {1.137}	{1.138}	{1.138}	(1.171) [1.143] {1.137}	{1.138}	{1.138}
C13-O3	(1.165) [1.138] {1.133}	{1.133}	{1.133}	(1.165) [1.138] {1.133}	{1.132}	{1.133}
Angle/ °						
Cl1-Ru-Cl2	(91.8) [91.5] {91.5}	{92.7}	{93.7}	(91.6) [91.3] {91.4}	{92.7}	{93.5}
Cl1-Ru-C12	(176.7) [176.8] {177.1}	{178.2}	{178.0}	(176.7) [176.8] {177.1}	{178.2}	{177.9}
Cl1-Ru-C11	(85.0) [85.4] {85.6}	{86.9}	{84.3}	(85.1) [85.5] {85.7}	{86.9}	{84.4}
Cl1-Ru-C13	(85.5) [86.2] {86.7}	{86.1}	{85.6}	(85.5) [86.3] {86.8}	{86.2}	{85.7}
Cl1-Ru-N3	(87.4) [87.2] {87.2}	{88.4}	{89.8}	(87.3) [87.1] {87.1}	{88.3}	{89.8}
Cl2-Ru-C12	(85.0) [85.4] {85.6}	{85.6}	{84.3}	(85.1) [85.5] {85.7}	{85.5}	{84.4}
Cl2-Ru-C11	(176.7) [176.8] {177.1}	{178.3}	{178.0}	(176.7) [176.8] {177.1}	{178.2}	{177.9}
Cl2-Ru-C13	(85.5) [86.2] {86.7}	{85.6}	{85.6}	(85.5) [86.3] {86.8}	{85.7}	{85.7}
Cl2-Ru-N3	(87.4) [87.2] {87.2}	{87.8}	{89.8}	(87.3) [87.1] {87.1}	{87.6}	{89.8}
C12-Ru-C11	(98.3) [97.7] {97.2}	{94.8}	{97.6}	(98.2) [97.6] {97.2}	{94.9}	{97.6}
C12-Ru-C13	(94.6) [94.1] {93.6}	{94.1}	{93.7}	(94. 6) [94.0] {93.5}	{94.0}	{93.7}
C12-Ru-N3	(92.0) [92.1] {92.2}	{91.2}	{90.7}	(92.1) [92.2] {92.3}	{91.3}	{90.7}
C11-Ru-C13	(94.6) [94.1] {93.6}	{92.6}	{93.7}	(94.6) [94.0] {93.5}	{92.5}	{93.6}
C11-Ru-N3	(92.0) [92.1] {92.2}	{93.9}	{90.7}	(92.1) [92.2] {92.3}	{94.1}	{90.7}
C13-Ru-N3	(169.8) [170.5] {171.3}	{171.2}	{173.3}	(169.7) [170.5] {171.2}	{171.2}	{173.3}

Ru-N3-C2	(120.3) [120.1] {120.2}	{122.3}	{124.8}	(120.3) [120.1] {120.1}	122.0}	{124.7}
Ru-N3-C9	(132.8) [133.4] {133.4}	{131.5}	{129.3}	(132.6) [133.2] {133.2}	{131.5}	{129.1}
Ru-C12-O2	(178.4) [178.6] {178.7}	{179.5}	{179.3}	(178.4) [178.6] {178.7}	{179.4}	{179.3}
Ru-C11-O1	(178.4) [178.6] {178.7}	{177.4}	{179.3}	(178.4) [178.6] {178.7}	{177.5}	{179.2}
Ru-C13-O3	(176.7) [177.5] {177.9}	{177.8}	{178.1}	(176.7) [177.5] {177.9}	{177.8}	{178.2}
N3-C2-N1	(111.8) [112.3] {112.4}	{112.7}	{113.0}	(111.2) [111.6] {111.7}	{112.0}	{112.3}
Cl1-Ru-N3-C2	(-45.9)[-45.8] {-45.8}	{-123.5}	{133.2}	(-45.9) [-45.7] {-45.8}	{-123.6}	{133.3}
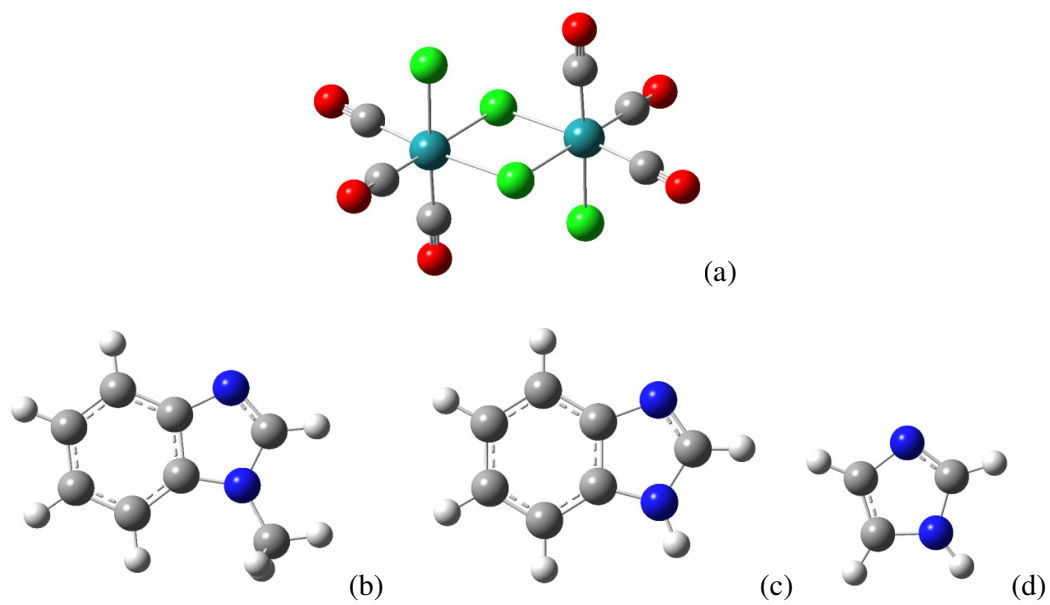
Figure S20. Computed structures of: (a) *fac,anti*-[Ru$^{II}_2$(CO)$_6$Cl$_4$], **1** (CORM2) at DFT-B3LYP/(Lanl2DZ,Ru;6-31G**, CClO); and (b) *N*-methylbenzimidazole, (c) benzimidazole, (d) imidazole at B3LYP/(Lanl2dz, Ru; 6-311++G**, CHClNO).
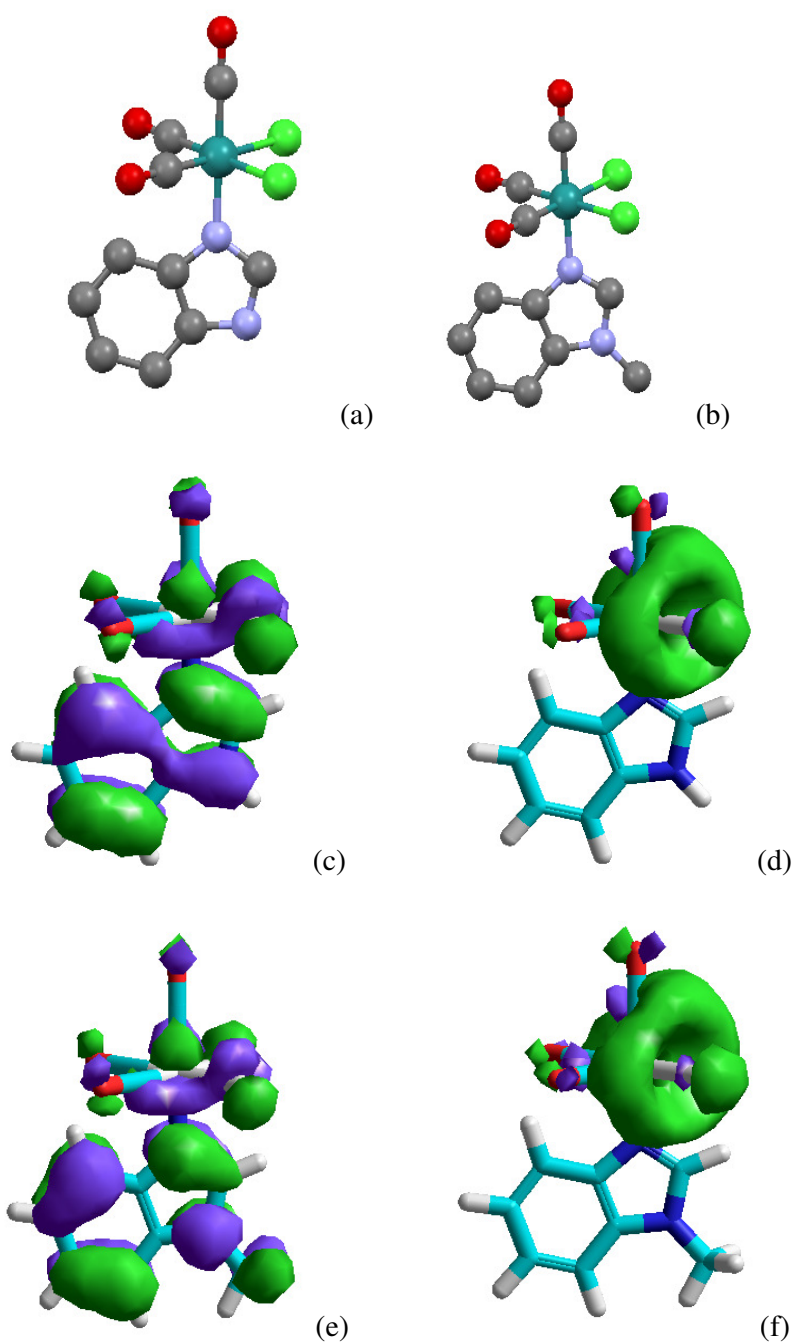
Figure S21. Diagram depicting a view for the type-A conformations as computed at ZINDO-1 level for: (a) *fac*-[Ru^{II}(CO)$_3$Cl$_2$($\underline{N}^3$-BIM)], (b) *fac*-[Ru^{II}(CO)$_3$Cl$_2$($\underline{N}^3$-MBI)]. The H atoms have been omitted. Diagrams depicting the molecular orbitals for optimized structures: *fac*-[Ru^{II}(CO)$_3$Cl$_2$($\underline{N}^3$-BIM)] type-A (c) HOMO and (d) LUMO; and *fac*-[Ru^{II}(CO)$_3$Cl$_2$($\underline{N}^3$-MBI)] type-A (e) HOMO, (f) LUMO.

Details on Spectrophotometric and ESI-MS Data
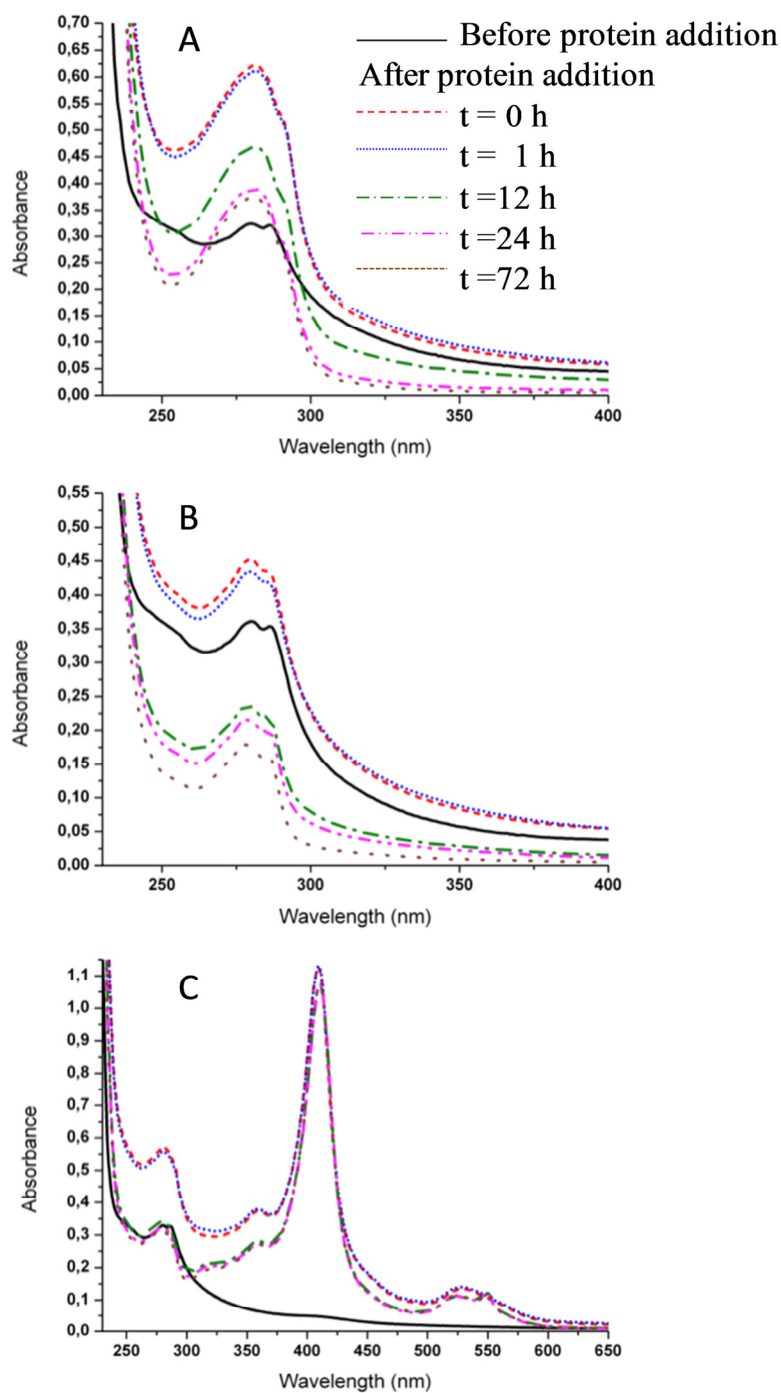
Figure S22. Time-course UV-Vis spectra of *fac*-[$Ru^{II}(CO)_3Cl_2(\underline{N}^3$-DMBI)], **4**, dissolved in 10 mM phosphate buffer (PB), pH 7.4, in the presence of HEWL (A), RNase A (B), Cyt c (C). Each solution contained 30 μM Ru and 10 μM protein.
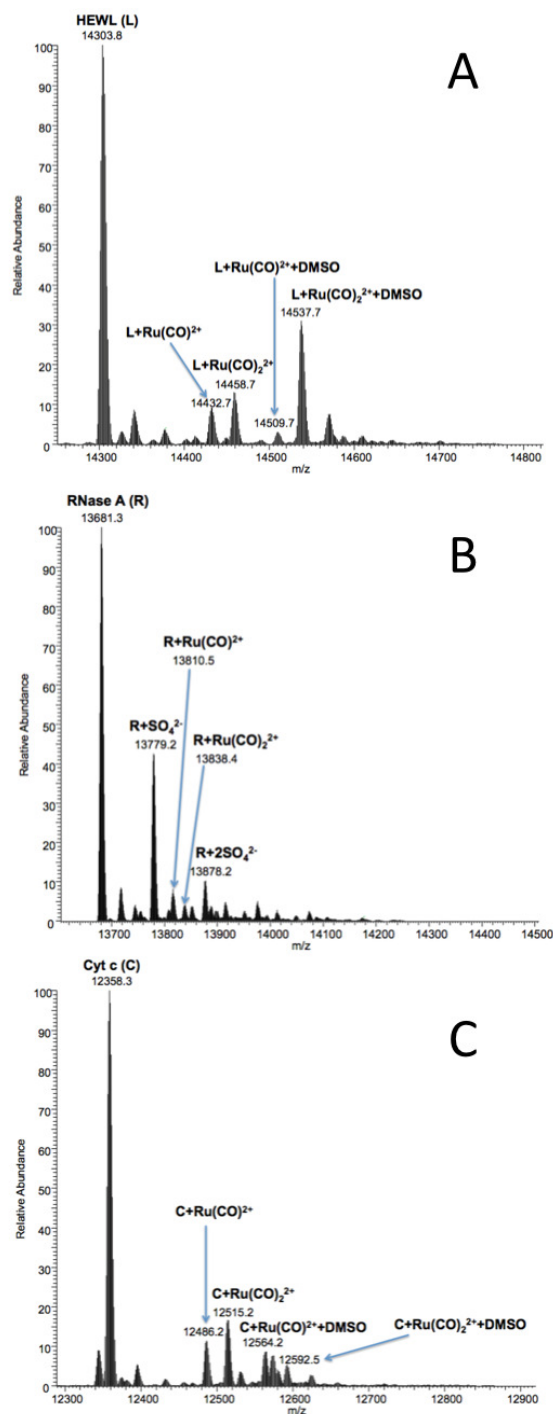
Figure S23. LTQ Orbitrap ESI mass spectra of **4** dissolved in 20 mM ammonium acetate buffer, pH 7.4, in the presence of HEWL (A), RNase A (B) or Cyt c (C) after 72 h of incubation at 37 °C. The protein concentration was 10^{-4} M (with a metal complex to protein molar ratio of 3:1).
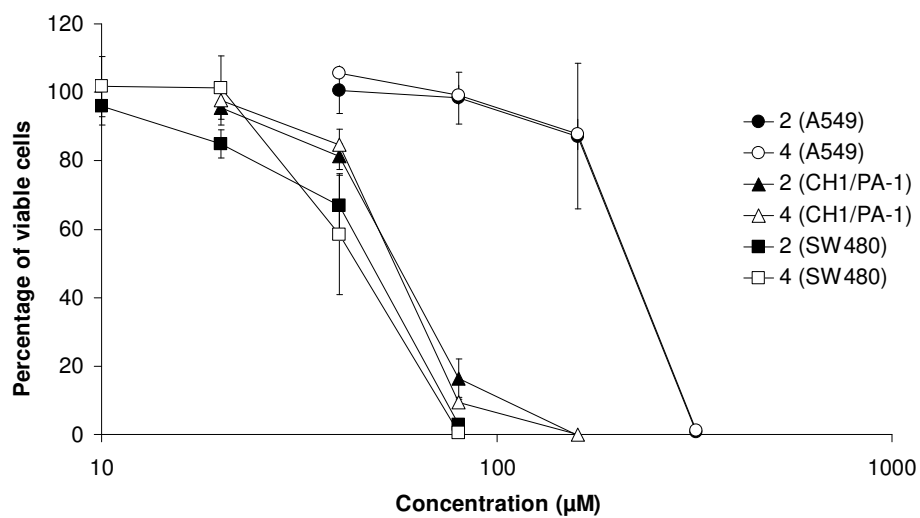
Cytotoxicity

Figure S24. Concentration–effect curves of **2** and **4** (from DMSO stocks) in three human cancer cell lines (A549, CH1/PA-1, SW480) in the MTT assay (96 h exposure).
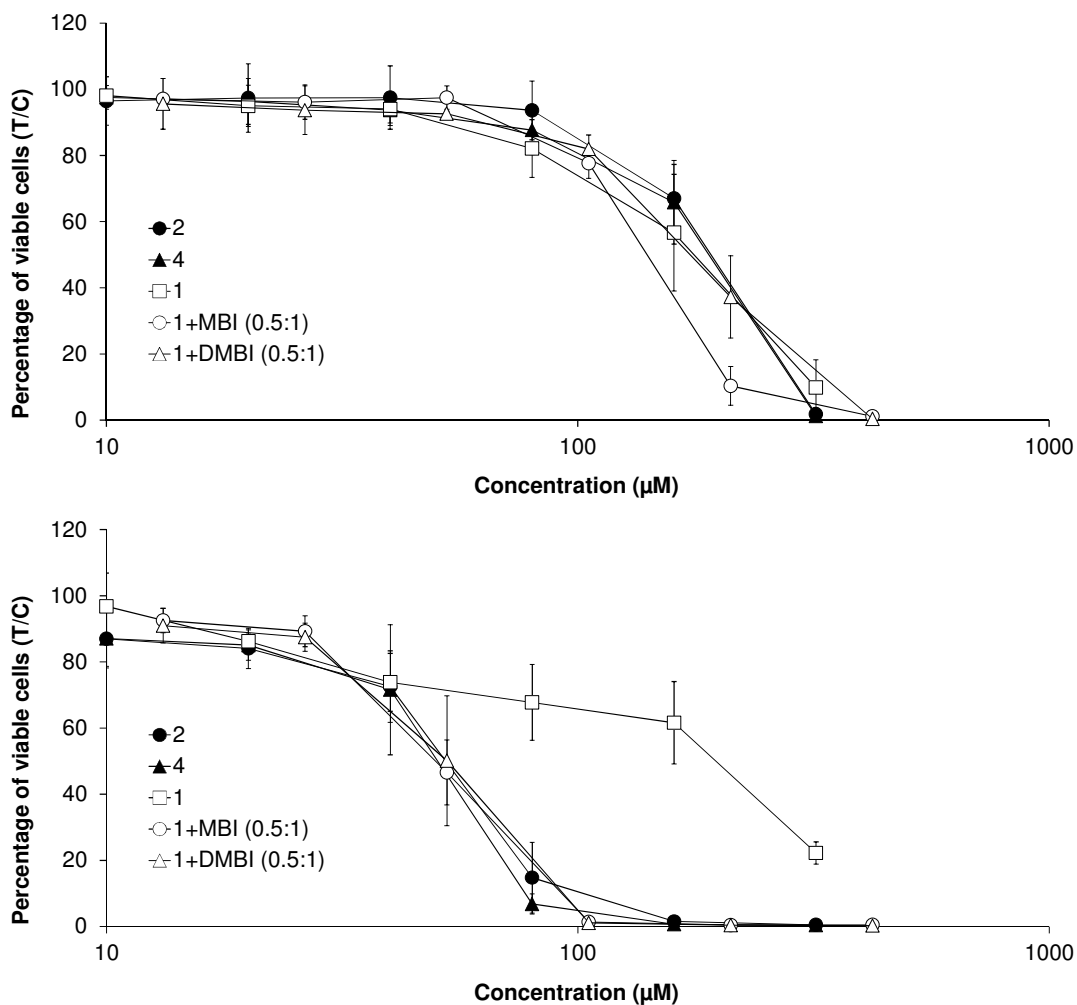
Figure S25. Concentration–effect curves of **2** and **4** as compared to **1** and 0.5:1 mixtures of **1** + MBI or DMBI (all from DMF stocks) in A549 (top) and SW480 cells (bottom) in the MTT assay (96 h exposure). Note that concentrations indicated for the mixtures relate to the molarities of MBI and DMBI, whereas the corresponding concentration of the dimeric **1** in the mixtures is half of that.